FRONTIERS OF PHYSICS

RESEARCH ARTICLE
Volume 21 / Issue 10 / 103202 / 2026

Robust optimization of two-qubit gates using the GRAPE algorithm in nitrogen–vacancy centers

Jun-Tong Ding[1,2], Xin-Yu Zhao[1,2,†], Ye-Hong Chen[1,2,3], Zhi-Cheng Shi[1,2,‡], Yan Xia[1,2,§]

1 Department of Physics, Fuzhou University, Fuzhou 350116, China
2 Fujian Key Laboratory of Quantum Information and Quantum Optics, Fuzhou University, Fuzhou 350116, China
3 Theoretical Quantum Physics Laboratory, RIKEN Cluster for Pioneering Research, Wako-shi, Saitama 351-0198, Japan
Corresponding authors. E-mail: †xzhao@fzu.edu.cn, ‡szc2014@yeah.net, §xia-208@163.com
Received September 13, 2025; accepted January 26, 2026

ABSTRACT

We propose a scheme for optimizing two-qubit gate operations in a decoherence-free subspace (DFS) using the gradient ascent pulse engineering (GRAPE) algorithm, where the system consists of nitrogen-vacancy (NV) centers in diamond coupled to a whispering-gallery-mode microresonator. The logical qubits in this scheme are encoded in the DFS, which effectively avoids collective decoherence and provides a long coherence time for high-fidelity quantum operations. The GRAPE algorithm is used to design and optimize the control pulse sequences required for the target operation, thereby compensating for common errors and ensuring that the quantum gate maintains high fidelity under non-ideal conditions. As examples, we successfully implement high-fidelity and robust controlled-phase and SWAP gates. Numerical simulations demonstrate the effectiveness and superiority of the proposed scheme. The strategy of combining encoding protection with optimal control shown in this work can be extended to implement universal quantum gates in complex quantum systems.

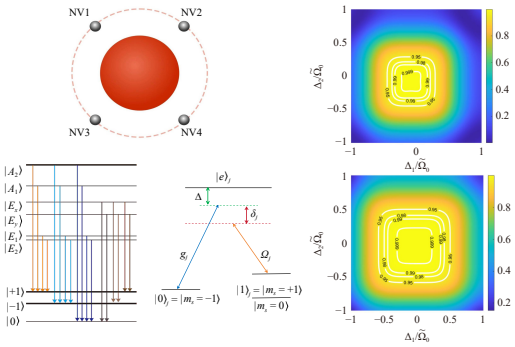

Keywords quantum computation, GRAPE algorithm, nitrogen–vacancy

1 Introduction

High-fidelity quantum computation forms the foundation for realizing cutting-edge technologies such as quantum information processing [1–4], quantum communication [5–8], and quantum sensing [9]. In recent years, research on quantum computation across various physical platforms has achieved remarkable progress in both theoretical and experimental aspects [10–19]. Realizing precise and reliable quantum computation typically requires addressing two main challenges: the decoherence induced by the inevitable interaction between the system and the environment, and the errors arising from the control process [20–22]. Several methods have been developed to overcome these obstacles, e.g., the construction of decoherence-free subspaces (DFSs) [23–29] and quantum optimal control [30–35].

The basic idea of DFS is to exploit the symmetry structure of the interaction between the system and the environment, thereby making quantum operations tolerant to decoherence effects induced by the environment [24]. Schemes for implementing quantum gates within DFS have been proposed in various physical systems, including nuclear magnetic resonance [36, 37], superconducting circuits [38–40], trapped ions [41–43], optical systems [44], and color centers in diamond [45–48]. Among these platforms, the nitrogen-vacancy (NV) centers in diamond are one of the promising candidates due to the

https://doi.org/10.15302/frontphys.2026.103202

superior optical and spin properties [49]. On the one hand, NV centers exhibit long electron spin coherence time even at room temperature, and quantum states can be readily initialized, manipulated, and read out via external laser and microwave fields [50–53]. On the other hand, whispering-gallery-mode (WGM) microcavities feature ultrahigh quality factors and small mode volumes. Coupling WGMs with NV centers can significantly enhance light–matter interactions and thus improve the photon–spin coupling efficiency [54–57], enabling the realization of fast and high-fidelity quantum gates.

In quantum optimal control, driving fields are typically determined via iterative methods to steer the system dynamics towards a predefined objective [58–62]. Until now, various efficient and robust numerical optimization methods have been developed, such as the gradient ascent pulse engineering (GRAPE) algorithm [63], stochastic gradient descent algorithm [64], and the Krotov method [65]. Among these, the GRAPE algorithm is especially notable for its efficiency in finding suitable solutions with fast convergence in parameter space. Compared with traditional analytical pulse designs [66, 67], the GRAPE algorithm is not limited to a specific form of the Hamiltonian and can naturally incorporate parameter constraints and noise models. To address the challenges of unavoidable decoherence and control noise, robust and stochastic GRAPE methods have been introduced [30, 68]. These methods systematically sample the error models and optimize the control pulses based on the performance of these samples, for example, the average fidelity. Such a design allows the resulting control strategies to exhibit high tolerance to frequency drifts, amplitude errors, and decoherence processes. In addition, high-speed GRAPE algorithms that combine parallel computing and GPU-based automatic differentiation make it possible to optimize hundreds of control parameters simultaneously, which greatly improves the efficiency of solving optimization problems in high-dimensional quantum systems [69–71]. Particularly, GRAPE algorithms combined with machine learning, such as those using deep neural networks to assist with initial pulse guesses or to adjust parameters online, can also reduce the dimensionality of the search space [72, 73].

In this work, we propose a scheme to optimize two-qubit gate operations using the GRAPE algorithm within DFS. The system consists of NV centers in diamond coupled to a WGM microresonator. Under large detuning conditions, only couplings between low energy states exist, making the scheme insensitive to the spontaneous emission of the NV centers. By restricting the system dynamics to the DFS, the qubits are protected from collective dephasing and other noise. On this basis, we use the GRAPE algorithm to effectively suppress the impact of systematic errors on quantum gates. Specifically, by optimizing an average objective function that accounts for various uncertainties, such as thermal noise and amplitude errors, the robustness of control can be significantly improved. The advantage of this scheme is that it can automatically search for optimal pulse sequences for any given target quantum gate. As specific applications, we implement robust controlled-phase and SWAP gates in NV centers coupled to a microsphere resonator. The results show that the two-qubit gates designed using this scheme maintain high fidelity even in the presence of thermal noise and amplitude errors.

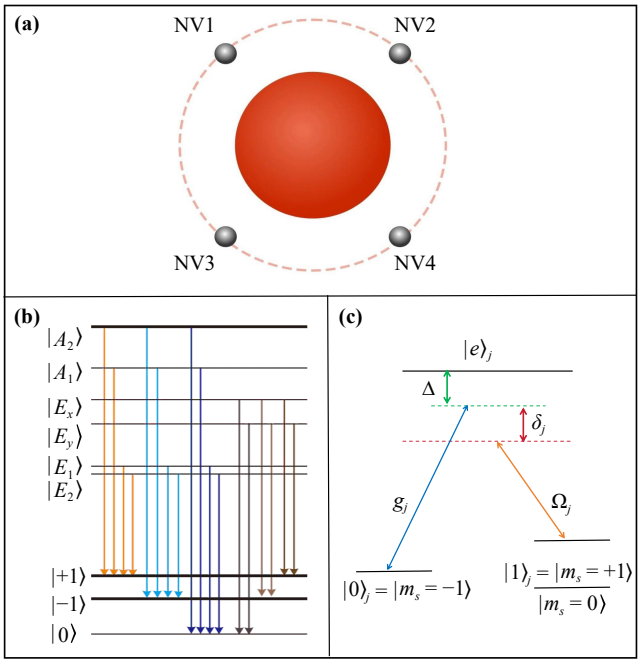

Fig. 1 Schematic of the system. **(a)** Four identical NV centers (silver dots) are equidistantly attached around the equator of a fused silica microsphere. **(b)** Energy-level structure of a single NV center in diamond. **(c)** Simplified energy-level diagram for the j-th NV center ($j = 1, 2, 3, 4$).

2 System Hamiltonian

As shown in Fig. 1(a), the system consists of four NV centers in diamond strongly coupled to the WGM of a fused-silica microsphere resonator. Each NV center is placed around the equator of the microsphere to ensure uniform and efficient interaction with the WGM. The energy-level structure of NV centers is shown in Fig. 1(b). The combined symmetry of the electronic and orbital structures determines that the ground state is a spin triplet state $|^3A_2\rangle$. In the absence of a magnetic field, there is a 2.88 GHz energy splitting between the levels $|m_s = \pm 1\rangle$ and $|m_s = 0\rangle$. The Coulomb interaction induces an optical transition between the ground and excited states with an energy gap of 469 THz [74], where the excited states include two spin–orbit doublet states

$|E_1\rangle$ and $|E_2\rangle$, two orbital doublet states $|E_x\rangle$ and $|E_y\rangle$, and two spin singlet states $|A_1\rangle$ and $|A_2\rangle$. When the nonaxial crystal strain is much smaller than the spin–orbit splitting, the combined effects of spin–orbit and spin–spin interactions lead to an energy splitting of at least 5.5 GHz between the state $|A_2\rangle$ and the other excited states [74]. The excited state $|A_2\rangle$ can decay by radiation of the left and right circular polarizations, with equal probability of jumping to $|m_s=-1\rangle$ and $|m_s=+1\rangle$ [75]. In this work, the basis states $|0\rangle$ and $|1\rangle$ of the qubit are encoded in the ground states $|^3A_2, m_s=-1\rangle$ and $|^3A_2, m_s=+1\rangle$ of the NV center, respectively. The excited state $|e\rangle$ corresponds to the orbital excited state $|A_2\rangle$. In this way, a Λ-type structure is established.

For the j-th NV center $(j=1,2,3,4)$, the transition between the ground state $|0\rangle_j$ and the excited state $|e\rangle_j$ is coupled to the WGM of the microsphere with frequency ω_c and coupling strength g_j, as shown in Fig. 1(c). Meanwhile, the transition between the ground state $|1\rangle_j$ and the excited state $|e\rangle_j$ is driven by a classical laser field with frequency $\omega_{L,j}$, phase ϕ_j, and Rabi frequency $\Omega_j/(2\pi)$. The total Hamiltonian of the system can be written as $(\hbar=1)$,

$$H=\omega_c a^\dagger a+\sum_{j=1}^{4}\Big[\sum_n \omega_n |n\rangle_j(n)+g_j a|e\rangle_j(0) + \Omega_j e^{-i(\omega_{L,j}t+\phi_j)}|e\rangle_j(1)\Big]+\text{H.c.}, \tag{1}$$

where $a^\dagger$ (a) is the creation (annihilation) operator for the WGM, ω_n is the energy of the n-th level of the NV center with $n\in\{0,1,e\}$, and H.c. denotes the Hermitian conjugate.

When both the coupling strength g_j and the Rabi frequency Ω_j are much smaller than the detuning $\Delta=\omega_e-\omega_0-\omega_c$, applying the rotating wave approximation and second-order perturbation theory [76], the Hamiltonian in the interaction picture can be written as

$$H_i=\sum_{j=1}^{4}\eta_j\left[a\sigma_j^+ e^{i(\delta_j t+\phi_j)}+\text{H.c.}\right], \tag{2}$$

with raising operator $\sigma_j^+=|1\rangle_j\langle 0|$, effective coupling strength $\eta_j=-\frac{1}{2}g_j\Omega_j\left(\frac{1}{\Delta-\delta_j}+\frac{1}{\Delta}\right)$, and effective detuning $\delta_j=\omega_1-\omega_0-\omega_c+\omega_{L,j}$.

Furthermore, when the laser fields selectively drive the m-th and r-th NV centers $(1\le m,r\le 4$ and $m\ne r)$ and the effective detuning δ_j is much larger than the effective coupling strength η_j, the Hamiltonian given by Eq. (2) can be simplified to [77]

$$H_C=\frac{\tilde{\Omega}_{mr}}{2}\left(e^{-i\varphi_{mr}}\sigma_m^-\sigma_r^+ +\text{H.c.}\right), \tag{3}$$

with effective Rabi frequency $\tilde{\Omega}_{m,r}=\eta_m\eta_r(1/\delta_m+1/\delta_r)$ and phase difference $\varphi_{mr}=\varphi_m-\varphi_r$. Here, we ignore the Stark shift which can be compensated by laser fields. As a result, by individually modulating the laser fields, it is possible to implement two-qubit gates in the NV centers.

3 Robust optimization of two-qubit gates based on DFS

In the current system, a major source of decoherence is collective decoherence. This type of noise arises since all NV centers are coupled to a shared environment. For example, the frequency ω_c of the microsphere resonator may slowly drift due to temperature variations, or the external magnetic field B_e may undergo global fluctuations. Although originating from different sources, these noise processes act in a similar way and can be described by a unified interaction Hamiltonian,

$$H_I=\left(\sum_{i=1}^{4}\sigma_z^i\right)\otimes B\equiv S_z\otimes B, \tag{4}$$

where $S_z=\sum_{i=1}^{4}\sigma_z^i$ is the total spin operator in the z-direction for the four NV centers. Since all qubits interact with the same environment B via the same operator S_z, any phase noise induced by B is identical for each eigenstate of S_z. Crucially, the construction of the DFS takes advantage of this symmetry. Therefore, an effective protection strategy can be constructed as long as this collective coupling structure persists.

To mitigate the collective decoherence described by Eq. (4), we can construct a six-dimensional DFS subspace using four NV centers [78]. The basis vectors for this subspace are

$$S=\{|0101\rangle,|0110\rangle,|1001\rangle,|1010\rangle,|0011\rangle,|1100\rangle\}. \tag{5}$$

Here, the first four basis vectors are selected to encode two logical qubits, which are defined as follows: $|00\rangle_L=|0101\rangle$, $|01\rangle_L=|0110\rangle$, $|10\rangle_L=|1001\rangle$, $|11\rangle_L=|1010\rangle$. The remaining two basis vectors, $|a_1\rangle=|0011\rangle$ and $|a_2\rangle=|1100\rangle$, are used as auxiliary states.

After constructing the noise-resistant DFS encoding, we proceed to achieve high-fidelity quantum logic gates within this subspace. As shown in Section 2, by precisely controlling external laser fields, one can induce effective interactions between the m-th and r-th NV centers, and the effective Hamiltonian in Eq. (3) can be rewritten as

$$H_C(t)=\frac{\tilde{\Omega}_{mr}(t)}{2}\left[e^{i\phi_{mr}(t)}|10\rangle_{mr}(01)\right]+\text{H.c.} \tag{6}$$

This Hamiltonian describes the selective transition $|01\rangle_{mr}\leftrightarrow|10\rangle_{mr}$ within the subspace formed by the m-th and r-th qubits.

It should be noted that although a simple pulse with a

specific pulse area can achieve target operations, it is highly sensitive to unavoidable parameter errors (e.g., laser power fluctuations), leading to poor gate fidelity. To overcome this difficulty, we employ the GRAPE algorithm to design pulse sequences that are robust against such errors. Within the framework of the GRAPE algorithm, directly optimizing $\phi_{mr}(t)$ is rather complicated. Therefore, we decompose the Hamiltonian (6) as follows:

$$H_C(t) = h_x(t)H_x + h_y(t)H_y, \tag{7}$$

where H_x and H_y are defined by

$$H_x = |10\rangle_{mr}(01) + |01\rangle_{mr}(10)\,, \tag{8}$$

$$H_y = \mathrm{i}\,(|10\rangle_{mr}(01) - |01\rangle_{mr}(10))\,. \tag{9}$$

The pulse amplitudes $h_x(t)$ and $h_y(t)$ are the updated parameters in the GRAPE algorithm [79], and they satisfy the constraint $h_x^2(t) + h_y^2(t) = \tilde{\Omega}_{mr}^2(t)$.

To optimize these pulse amplitudes, we need to define an objective function that quantifies the robustness of the performance. A straightforward selection of the objective function is as follows:

$$\bar{\Phi}(h_x, h_y) = \sum_i w_i\, \Phi(h_x, h_y, \epsilon_i), \tag{10}$$

where we sample the errors, w_i are the normalized weights associated with each sample ϵ_i, and $\Phi(h_x, h_y, \epsilon_i)$ represents the gate fidelity in the presence of a specific error ϵ_i. This fidelity is defined as

$$\Phi(h_x, h_y, \epsilon_i) = \frac{\left|\mathrm{Tr}[U_F^\dagger U(T, \epsilon_i)]\right|^2}{\mathrm{Tr}(P_{\mathrm{DFS}})^2}. \tag{11}$$

Here, U_F and $U(T, \epsilon_i)$ are the target and actual quantum gate at total evolution time T in the presence of error ϵ_i, respectively, and P_{DFS} represents the projective operator of the DFS on the system Hilbert space. That is, this objective function represents a weighted average fidelity of error samples.

We incorporate the objective function $\bar{\Phi}(h_x, h_y)$ into the robust optimization framework based on the GRAPE algorithm, in which the total evolution time T is divided into N pulse segments of equal duration τ, and the control amplitudes $h_{x,n}$ and $h_{y,n}$ are kept constant during the n-th segment, $n = 1, \cdots, N$. The key of this algorithm is to iteratively update these control amplitudes by gradient ascent. In the k-th iteration, we calculate the gradient of the objective function $\bar{\Phi}(h_x, h_y)$ with respect to each control amplitude. Since $\bar{\Phi}(h_x, h_y)$ is a weighted sum of fidelities over the error samples, its gradient is correspondingly the weighted sum of the individual gradients:

$$\bar{g}_{x,n}^{(k)} = \frac{\partial \bar{\Phi}(h_x, h_y)}{\partial h_{x,n}} = \sum_i w_i \frac{\partial \Phi(h_x, h_y, \epsilon_i)}{\partial h_{x,n}}, \tag{12}$$

$$\bar{g}_{y,n}^{(k)} = \frac{\partial \bar{\Phi}(h_x, h_y)}{\partial h_{y,n}} = \sum_i w_i \frac{\partial \Phi(h_x, h_y, \epsilon_i)}{\partial h_{y,n}}. \tag{13}$$

Subsequently, the control amplitudes are updated along the direction of this average gradient to enhance the average fidelity,

$$h_{x,n}^{(k+1)} = h_{x,n}^{(k)} + \lambda\, \bar{g}_{x,n}^{(k)}, \tag{14}$$

$$h_{y,n}^{(k+1)} = h_{y,n}^{(k)} + \lambda\, \bar{g}_{y,n}^{(k)}, \tag{15}$$

where the positive real number λ is learning rate and determines the step size of each iteration. Through this iterative process, an optimal set of pulse sequences for amplitudes $h_{x,n}$ and $h_{y,n}$ that actively compensate for the errors is obtained, thereby implementing highly robust target quantum operations.

4 Numerical simulations

In this section, we apply the robust optimal control framework established in the previous section to design two common two-qubit logic gates: the controlled-phase gate and the SWAP gate.

4.1 Controlled-phase gate

We first adopt the robust optimization method to achieve a controlled-phase gate denoted by G_P. Unlike a conventional controlled-phase gate, the G_P gate designed in our model applies an identical geometric phase ϑ to the logical basis states $|00\rangle_L$ and $|11\rangle_L$, while keeping $|01\rangle_L$ and $|10\rangle_L$ unchanged. The matrix form of G_P in the basis $\{|00\rangle_L, |01\rangle_L, |10\rangle_L, |11\rangle_L\}$ is given by

$$G_P = \begin{pmatrix} \mathrm{e}^{\mathrm{i}\vartheta} & 0 & 0 & 0 \\ 0 & 1 & 0 & 0 \\ 0 & 0 & 1 & 0 \\ 0 & 0 & 0 & \mathrm{e}^{\mathrm{i}\vartheta} \end{pmatrix}. \tag{16}$$

It should be noted that G_P can be recovered to a conventional controlled-phase gate by performing appropriate local single-qubit operations.

To obtain G_P, we drive the second and third NV centers by laser fields to induce virtual excitation processes between the logical basis states and the auxiliary states. There are two parallel and independent evolution channels during system dynamics, and the effective control Hamiltonian $H_C(t)$ is given by

$$H_C(t) = \frac{\tilde{\Omega}(t)}{2}\left[\mathrm{e}^{\mathrm{i}\varphi_{32}(t)}\,|a_1\rangle_L(00) + \mathrm{e}^{\mathrm{i}\varphi_{23}(t)}\,|a_2\rangle_L(11)\right] + \mathrm{H.c.}, \tag{17}$$

where the phase difference $\varphi_{32}(t)$ can be precisely controlled by the laser fields. When the pulse area satisfies $\tilde{\Omega}(t)\tau = \pi$, the logical basis states $|00\rangle_L$ and $|11\rangle_L$ individually complete a cyclic evolution and thus accumulate an additional phase ϑ. According to Eq. (17), we also find that both logical basis states $|01\rangle_L$ and $|10\rangle_L$ are not coupled to any states. Therefore, they remain unchanged throughout the entire evolution process.

To make the target gate G_P robust against parameter errors, we then employ the GRAPE algorithm to design the phase difference $\varphi_{32}(t)$, and rewrite the effective control Hamiltonian (17) as

$$H_C(t) = h_x(t)H_x + h_y(t)H_y, \tag{18}$$

$$H_x = \frac{1}{2}\left(|a_1\rangle_L(00) + |a_2\rangle_L(11) + \text{H.c.}\right), \tag{19}$$

$$H_y = \frac{\mathrm{i}}{2}\left(|a_1\rangle_L(00) + |a_2\rangle_L(11) + \text{H.c.}\right), \tag{20}$$

where the amplitudes satisfy $h_x^2(t) + h_y^2(t) = \tilde{\Omega}^2(t)$. By considering uncertainties such as Rabi frequency errors and thermal noise, we numerically solve for the optimal pulse sequences of $h_x(t)$ and $h_y(t)$. The resulting pulse sequences not only ensure the closure of the evolution path to eliminate the dynamical phase but also effectively compensate for the influence of various systematic errors.

$$\tilde{\Omega}'(t) = (1+\delta)\tilde{\Omega}(t), \tag{21}$$

where $\tilde{\Omega}(t)$ is the nominal Rabi frequency and the dimensionless parameter δ indicates the degree of deviation of the actual Rabi frequency $\tilde{\Omega}'(t)$ from its nominal value. For simplicity, we assume δ is a constant hereafter.

As shown in Fig. 2, we plot the gate fidelity F of the obtained controlled-phase gate G_P as a function of the Rabi frequency error δ. From the curve corresponding to $N = 4$ in which the control pulse parameters are listed in Table 1, it can be seen that even when δ varies over a wide range of $-0.4 < \delta < 0.4$, the fidelity remains above 0.98. In the small range of $\delta \in [-0.1, 0.1]$, the fidelity can exceed 0.9999, demonstrating the excellent robustness of this control scheme against Rabi frequency errors. Note that the fidelity can still reach about 0.84 even when the error is the same as the target Rabi frequency. This results from the specificity of the G_P gate which is a near-identity diagonal operator in the DFS space. Thus, the focus should be on the high-fidelity window (e.g., $F \geq 0.9999$) for the G_P gate to demonstrate the effectiveness of the current algorithm in mitigating the error δ.

In this optimization framework, the control pulse is discretized into N time segments. The number of segments is a key parameter affecting the final control performance, as it is crucial for ensuring that the implemented geometric gate automatically cancels the dynamical phase and satisfies the closure of the evolution path. A larger value of N provides more degrees of freedom for control, enabling the optimization algorithm to fine-tune the control strategy more meticulously. As a result, the resilience to errors is also enhanced for the system. Figure 2 also displays the trend of the fidelity F as a function of the Rabi frequency error δ for different values of N. The results show that the high-fidelity plateau becomes wider as N increases. In particular, in the region of small errors, e.g., $|\delta| < 0.2$, the overall fidelity remains at a relatively high level. Note that the peak fidelity slightly shifts from $\delta = 0$ for most N, as the current algorithm prioritizes maximizing the average fidelity over the error range, trading the peak performance for a broader plateau. To obtain high fidelity at $\delta = 0$, a

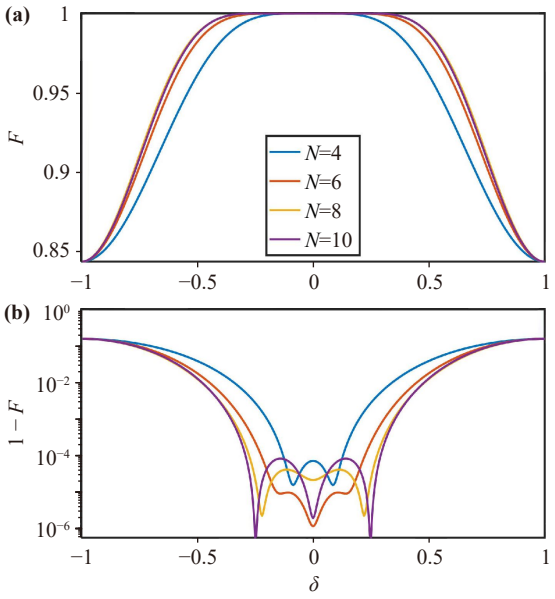

Fig. 2 **(a)** Fidelity F and **(b)** infidelity $1-F$ of the controlled-phase gate G_P vs Rabi frequency error δ. The duration of a single pulse segment is $\tau = \pi/\tilde{\Omega}(t)$ with $\tilde{\Omega}(t)$ keeping unchanged, the target phase reads $\vartheta = 0.5$, and the total evolution time is $T = N\tau$. The learning rate is $\epsilon = 0.001$, and the robust optimization is performed over 1000 error samples. It can be found that the system can maintain high fidelity within a large error range as the number of pulse segments N increases.

Table 1 Pulse sequences for the controlled-phase gate optimized against different errors ($N = 4$, in units of $\tilde{\Omega}_0$).

n	Rabi frequency error		Thermal noise	
	$h_x(n)$	$h_y(n)$	$h_x(n)$	$h_y(n)$
1	0.0373	−0.9993	0.4987	−0.8668
2	0.2085	0.9780	0.2511	−0.9680
3	0.4556	0.8902	−0.1061	−0.9944
4	−0.6748	−0.7380	−0.3454	−0.9385

feasible approach is to perform multiple samplings near $\delta = 0$ in the GRAPE algorithm.

Next, we analyze the robustness of the controlled-phase gate G_P against thermal noise. At room temperature, the orientations of nuclear spins are randomly distributed. The perturbations arising from these thermal fluctuations can be treated as a form of thermal noise, which is characterized by slow variations (quasi-static) and can be regarded as constant over a gate operation period [80]. Thermal noise typically limits the coherence time of NV centers to the microsecond scale, but due to its low-frequency nature, it can be effectively suppressed by refocusing techniques such as spin echo [81]. However, this type of noise can still lead to a degradation in the fidelity of quantum gate operations and thus should be considered during the optimization process. As previously discussed, the DFS encoding provides perfect protection against ideal collective decoherence noise. In practice, noise sources may not be perfectly symmetric, leading to compromise the protective capability of the DFS.

Note that the thermal noises acting on the two transitions, $|00\rangle_L \leftrightarrow |a_1\rangle$ and $|11\rangle_L \leftrightarrow |a_2\rangle$, may not be fully correlated. This asymmetry originates from subtle differences in the environment surrounding each NV center, such as independent fluctuations in local magnetic or electric fields. To more rigorously evaluate the performance of our scheme, we construct an asymmetric noise model where two independent thermal noise strengths, Δ_1 and Δ_2, are modeled as energy detunings for these two transition channels. The effective noise Hamiltonian can be written as

$$H_{\text{noise}} = \frac{\Delta_1}{2}\left(|a_1\rangle(a_1| - |00\rangle_L(00|_L\right) + \frac{\Delta_2}{2}\left(|a_2\rangle(a_2| - |11\rangle_L(11|_L\right). \tag{22}$$

Figure 3 shows the robustness of the gate fidelity against thermal noise strengths Δ_1 and Δ_2 for different numbers of pulse segments, where the control pulse parameters for $N = 4$ are presented in Table 1. We can clearly see a central high-fidelity region where both Δ_1 and Δ_2 are zero. As the number of pulse segments N increases, the area of this high-fidelity region expands, and the fidelity distribution within it becomes flatter. Specifically, the region with fidelity above 0.999 is relatively small for $N = 4$, whereas this high-fidelity region covers almost the entire square parameter space from -0.1 to 0.1 when increased to $N = 8$. This result demonstrates that increasing the degrees of control freedom (i.e., increasing N) enables the GRAPE algorithm to find more optimal control solutions that actively compensate for asymmetric noise over a broader range. One can also observe that the fidelity contours is asymmetric with respect to the distribution of thermal noises. The reason can be understood as follows. First, the presence of thermal

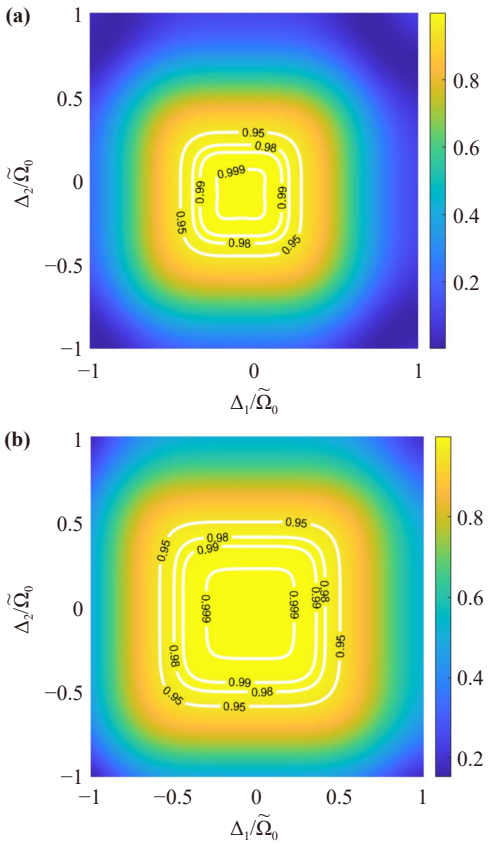

Fig. 3 Robustness of the controlled-phase gate against variations in thermal noises $\Delta_1/\tilde{\Omega}_0$ and $\Delta_2/\tilde{\Omega}_0$ for different pulse segments. **(a)** $N = 4$. **(b)** $N = 8$. The central region of near-unit fidelity outlined by the contour lines expands as N increases. This indicates that increasing the control degrees of freedom enables the optimization algorithm to find favorable control solutions, thereby effectively compensating for asymmetric noise over a wide region.

noises break the symmetry of the system dynamics, causing the optimization to converge on control solutions that compensate for energy shifts asymmetrically. Second, the current algorithm utilizes randomly initial pulses. While the final result converges on the locally optimal solution, the optimization path is influenced by the initial selection, potentially biasing the compensation to be more effective for certain directions of thermal noises. This might also contribute to the asymmetrical feature of the final fidelity curve.

Finally, we compare the performance of the robust optimization strategy proposed in this work with that of nonadiabatic noncyclic geometric quantum computation (NNGQC) [82] for implementing a controlled-phase gate. The NNGQC method leverages the inherent robustness of the geometric phase, providing it with natural resilience against certain types of global noise [82]. The performance of this method is highly dependent on the precise implementation of analytical pulse shapes and is consequently sensitive to deviations in some parameters.

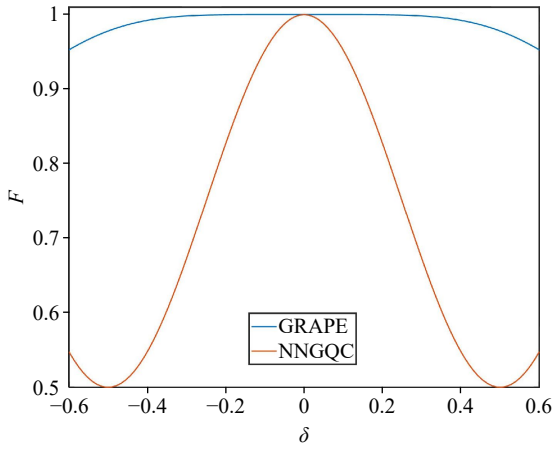

Fig. 4 Robustness of the controlled-phase gate against Rabi frequency error δ for the robust GRAPE and NNGQC scheme [82]. We here use pulse segments $N = 6$ and a total gate time of $3\pi/\tilde{\Omega}_0$, while the peak Rabi frequency is set to $\tilde{\Omega}_0/(2\pi) = 10\,\text{MHz}$ and the total gate time is $2\pi/\tilde{\Omega}_0$ for the NNGQC scheme.

In contrast, our GRAPE-based framework is a numerical optimization method that compensates for specific errors by maximizing an objective function that incorporates a range of error samples. As shown in Fig. 4, our method with $N = 6$ significantly enhances the gate fidelity over a large error range. Particularly in the small error regime of $\epsilon \in [-0.1, 0.1]$, it maintains a fidelity greater than 0.9999, forming a broad high-fidelity plateau. In contrast, the fidelity of the NNGQC scheme deteriorates as the error deviates from zero. The root of this performance difference lies in the fact that our algorithm, by exploring a high-dimensional control space, identifies a flat optimal region that is insensitive to Rabi frequency fluctuations, whereas the analytical solution of NNGQC corresponds to a sharp optimum that is susceptible to parameter variations.

4.2 SWAP gate

The SWAP gate is a common and crucial two-qubit gate to construct complex quantum circuits in quantum computation. The action of the SWAP gate is to exchange the states of two qubits, and its matrix representation in the logical qubit subspace S_1 can be represented as

$$U_{\text{SWAP}} = \begin{pmatrix} 1 & 0 & 0 & 0 \\ 0 & 0 & 1 & 0 \\ 0 & 1 & 0 & 0 \\ 0 & 0 & 0 & 1 \end{pmatrix}. \tag{23}$$

Here, we propose a two-step synthesis scheme that follows the robust optimization framework presented in Section 3 but decomposes the complex task into two more manageable steps.

In the first step, the laser fields selectively act on the first and second NV centers, and on the third and fourth NV centers, respectively. The control Hamiltonian of the system is

$$\begin{aligned} H_1(t) = \frac{\tilde{\Omega}(t)}{2}\Big[& e^{i\phi_{12}(t)}\big(|10\rangle_L(00) + |11\rangle_L(01)\big) \\ & + e^{i\phi_{34}(t)}\big(|01\rangle_L(00) + |11\rangle_L(10)\big)\Big] + \text{H.c.}. \end{aligned} \tag{24}$$

It is easy to verify from Eqs. (6) and (24) that the evolution processes driven by the laser fields on the first/second and third/fourth NV centers are mutually independent and do not affect each other. This means that, we can drive the first and second NV centers first, followed by the third and fourth NV centers, without altering the final evolution operator. When $\tilde{\Omega}(t)\tau_1 = \pi/2$, the matrix form for the evolution operator in the basis $\{|a_1\rangle, |00\rangle_L, |01\rangle_L, |10\rangle_L, |11\rangle_L, |a_2\rangle\}$ becomes

$$U_1 = \begin{pmatrix} 1 & 0 & 0 & 0 & 0 & 0 \\ 0 & 0 & 0 & 0 & 1 & 0 \\ 0 & 0 & 0 & e^{i\vartheta} & 0 & 0 \\ 0 & 0 & e^{i\vartheta} & 0 & 0 & 0 \\ 0 & 1 & 0 & 0 & 0 & 0 \\ 0 & 0 & 0 & 0 & 0 & 1 \end{pmatrix}. \tag{25}$$

To make the evolution operator U_1 robust against systematic errors, we employ the robust optimal control framework based on the GRAPE algorithm. Specifically, we set U_1 as the target operation U_F in the objective function (11) and search for the optimal time-varying amplitudes $h_{1x}(t)$ and $h_{1y}(t)$ corresponding to the control Hamiltonians H_{1x} and H_{1y}, where

$$\begin{aligned} H_{1x} = \frac{1}{2}\big(& |10\rangle_L(00) + |01\rangle_L(00) \\ & + |11\rangle_L(01) + |11\rangle_L(10)\big) + \text{H.c.}, \end{aligned} \tag{26}$$

$$\begin{aligned} H_{1y} = \frac{i}{2}\big(& |10\rangle_L(00) + |01\rangle_L(00) \\ & + |11\rangle_L(01) + |11\rangle_L(10)\big) + \text{H.c.}. \end{aligned} \tag{27}$$

Note that the condition $h_{1x}^2(t) + h_{1y}^2(t) = \tilde{\Omega}^2(t)$ is always met during the evolution process.

Next, the laser field selectively acts on the second and third NV centers, as well as the first and fourth NV centers. The control Hamiltonian of the system then becomes

$$\begin{aligned} H_2(t) = \frac{\tilde{\Omega}(t)}{2}\Big[& e^{i\phi_{23}(t)}\big(|a_1\rangle_L(00) + |a_2\rangle_L(11)\big) \\ & + e^{i\phi_{14}(t)}\big(|a_2\rangle_L(00) + |a_1\rangle_L(11)\big)\Big] + \text{H.c.}. \end{aligned} \tag{28}$$

Similar to the first step, when $\tilde{\Omega}(t)\tau_2 = \pi/2$, the evolution operator in DFS reads

$$U_2 = \begin{pmatrix} 0 & 0 & 0 & 0 & 0 & 1 \\ 0 & 0 & 0 & 0 & 1 & 0 \\ 0 & 0 & e^{i\vartheta} & 0 & 0 & 0 \\ 0 & 0 & 0 & e^{i\vartheta} & 0 & 0 \\ 0 & 1 & 0 & 0 & 0 & 0 \\ 1 & 0 & 0 & 0 & 0 & 0 \end{pmatrix}. \tag{29}$$

The robust control sequence for the second step is obtained by performing a new, independent round of GRAPE optimization. In this stage, the target operation becomes U_2 and we substitute it into the objective function (11). We iteratively update the time-varying amplitudes $h_{2x}(t)$ and $h_{2y}(t)$ for the corresponding control Hamiltonians H_{2x} and H_{2y},

$$H_{2x} = \frac{1}{2}\Big[\big(|a_1\rangle_L + |a_2\rangle_L\big)\big((00)+(11)\big) + \text{H.c.}\Big], \tag{30}$$

$$H_{2y} = \frac{i}{2}\Big[\big(|a_1\rangle_L + |a_2\rangle_L\big)\big((00)+(11)\big) + \text{H.c.}\Big], \tag{31}$$

to maximize the average fidelity over errors, thereby yielding the optimal pulse sequences. After these two steps, we finally obtain a robust SWAP gate given by

$$U_{\text{SWAP}} = U_2\, U_1. \tag{32}$$

By decomposing the complex SWAP gate task into two more easily controllable and optimizable steps, we provide an alternative pathway for realizing high-fidelity and robust quantum gates. The decomposition strategy demonstrates the flexibility of our optimization framework, allowing a complex task to be broken down into several independently optimizable subtasks to efficiently achieve the overall goal.

To quantitatively evaluate the effectiveness of the designed control strategy, we examine the robustness of the final synthesized gate U_{SWAP} against Rabi frequency errors, where the actual Rabi frequency $\tilde{\Omega}'(t)$ is related to the nominal frequency $\tilde{\Omega}(t)$ by

$$\tilde{\Omega}'(t) = (1+\delta)\tilde{\Omega}(t). \tag{33}$$

Figure 5 shows the fidelity F of the gate U_{SWAP} as a function of the Rabi frequency error δ in which the control pulse parameters for $N = 10$ are listed in Table 2. For the case of $N = 10$ (the blue curve), the fidelity remains at a high level ($F > 0.9$) within the error range $\delta \in [-0.4, 0.4]$, and exceeds 0.9999 in a small perturbation range (e.g., $\delta \in [-0.1, 0.1]$). This demonstrates that the composite SWAP gate obtained through our step-wise optimization exhibits excellent robustness against Rabi frequency errors.

Next, we further investigate the effect of the total number of pulse segments on the robustness of the U_{SWAP} gate. Here, N represents the total length of the control pulse sequence for the entire U_{SWAP} gate, which is evenly distributed between the two subgates U_1 and U_2 (i.e., each sub-gate has $N/2$ segments). To systematically evaluate this effect, we also display the fidelity F and infidelity $1-F$ of the final composite gate U_{SWAP} as a function of the error δ for different pulse segments N in Fig. 5.

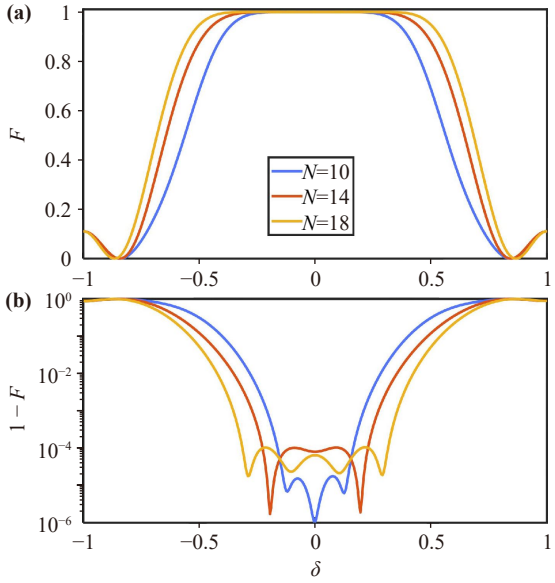

Fig. 5 Effect of different numbers of pulse segments on the robustness of the gate U_{SWAP}. **(a)** Fidelity F and **(b)** infidelity $1-F$ vs. Rabi frequency error δ. The gate U_{SWAP} is composed of two sub-gates with an equal number of segments, where the duration of a single pulse segment is $\tau = \pi/[2\tilde{\Omega}(t)]$ with $\tilde{\Omega}(t)$ keeping unchanged, and the total evolution time is $T = 2N\tau$. The learning rate is $\epsilon = 0.001$, and the robust optimization is performed over 1000 error samples.

As shown in Fig. 5, increasing the number of pulse segments N can significantly improve the robustness. To be specific, when N increases from 10 to 18, the fidelity becomes increasingly flat around $\delta = 0$, and the error tolerance window for maintaining high fidelity is also significantly broadened. For instance, for $N = 18$ (the purple curve), the fidelity forms a near-perfect plateau

Table 2 Pulse sequences for the stepwise implementation of the SWAP gate with $N = 10$ (in units of $\tilde{\Omega}_0$). The optimization is averaged over 1000 error samples uniformly drawn from $\delta \in [-1, 1]$, where the learning rate is $\epsilon = 0.001$, and the duration of each pulse segment is $\tau = \pi/(2\tilde{\Omega}_0)$.

n	$h_{1x}(n)$	$h_{1y}(n)$	$h_{2x}(n)$	$h_{2y}(n)$
1	−0.9791	0.2034	−0.3885	0.9215
2	−0.0484	−0.9988	0.9883	−0.1524
3	0.9595	0.2818	−0.0357	−0.9994
4	−0.6735	−0.7392	0.4829	0.8757
5	−0.7632	−0.6461	0.8518	0.5238

over the broad range of $\delta \in [-0.2, 0.2]$, demonstrating excellent robustness. The logarithmic figure of infidelity more clearly reveals that the peak fidelity (at $\delta = 0$) does not sharply increase with N. In particular, for the cases of $N = 14$ and $N = 18$, distinct flat structures appear around $\delta = \pm 0.2$. This indicates that the optimization algorithm actively compensates for the effects of non-zero errors, trading a slight decrease in peak performance for robust high-fidelity control over a wider parameter tolerance range. Thus, increasing the number of pulse segments for each sub-gate is a key strategy for enhancing the robustness of the final composite gate U_{SWAP}. A large number of control segments provides a rich parameter space for optimization algorithm, allowing it to discover more refined and complex control strategies to effectively counteract the impact of systematic errors. These results clearly demonstrate that our GRAPE-based optimization strategy is capable of achieving not only a high-fidelity U_{SWAP} gate but also exhibits excellent robustness against systematic errors.

5 Disscusion

In addition to the GRAPE algorithm, there are currently many other methods for achieving robust quantum gates, such as composite pulse methods [83–85] and the single-shot pulse method [86, 87].

The advantage of composite pulse methods [83–85] lies in the ability to effectively compensate for any systematic errors, including pulse amplitude, pulse duration, and Stark shifts, etc. Therefore, this method holds wide applications in quantum computations. However, as the number of pulses increases, the series expansion of the fidelity with respect to errors becomes overly complex, which may prevent finding a satisfactory set of solutions that are robust to systematic errors.

The single-shot pulse method [86, 87] utilizes perturbation theory, such as the Dyson expansion, to expand the fidelity with respect to noises. The sensitivity to noises can be reduced by properly designing pulse waveforms. The strength of this method is that it confines the complexity of the system to be controlled within a certain range, allowing the use of analytical or geometric approaches to derive pulse waveforms. Nevertheless, robustness against different orders of noises requires to redesign the pulse waveform each time, and the corresponding waveform becomes increasingly complex and unconventional, which may pose challenges for experimental implementation.

The GRAPE algorithm [63] searches for optimal parameters by following the direction that increases the average fidelity. Thus, this method has a very high search efficiency and can obtain local optima in a short period of time. The potential drawback is that it may easily fall into local optima. To address this issue, we employ random initialization of multiple sets of parameters and select random gradient ascent directions for parameter updates, thereby obtaining multiple sets of optimal solutions in parallel. Then, the optimal robust solution is ultimately determined by comparing the robustness of these solutions.

Note that the GRAPE algorithm used in this work differs slightly from the traditional GRAPE algorithm. In the original algorithm [63], to ensure its convergence, the pulse step size is typically chosen to be small such that the first-order approximation remains valid. This directly results in a large number of pulses to be optimized, which in turn affects the rapid convergence of the algorithm. In this work, the pulse step size is designed to be relatively large, satisfying $\tau = \pi/\tilde{\Omega}_0$. As a result, only a small number of pulses need to be optimized to achieve robust control, which is more conducive to experimental implementation and faster convergence of the GRAPE algorithm. It is worth emphasizing that the convergence of the current algorithm is ensured through well-designed pulse durations rather than small pulse step sizes.

It is worth noting that the current optimization scheme is designed based on the Hamiltonian (3). Whether the Hamiltonian (3) can well describe the system dynamics of the NV centers coupled the WGM resonator needs to be verified. To this end, we plot in Fig. 6 the time evolution of the fidelity for the controlled-phase gate under $N = 4$ using the Hamiltonian (1) and Hamiltonian (3), respectively. In numerical simulations, we adopt the coupling strength to $g/(2\pi) = 700\,\mathrm{MHz}$, corresponding to the strong coupling regime accessible in whispering-gallery-mode resonator with high quality factors and small mode volumes [88–90]. We can observe from Fig. 6 that the fidelities of the two curves almost overlap and approach unit at the end of the pulse, demonstrating the validity of this approximation process. It should be mentioned that the two curves deviate during the time evolution, mainly due to the fact that we ignore the Stark shift in the Hamiltonian (3). Under these parameters, the operation time of the controlled-phase gate is approximately 3.5 μs, much shorter than the typical electron spin coherence time of NV centers ($T_2 > 10$ μs) [91]. In addtion, the current scheme only requires a simple square wave, and each segment lasts for 0.875 μs for $N = 4$, which can be easily generated by a waveform generator.

The precise positioning of nanodiamonds and the stability of the cavity (laser field) frequency may be challenging in experiments, leading to the fidelity of quantum gates drops. Note that the deviation of the nondiamond position is reflected in the deviation of the effective Rabi frequency while the shift of the cavity (laser field) frequency will be reflected in the thermal noise in the current model. Thus, the influence of those

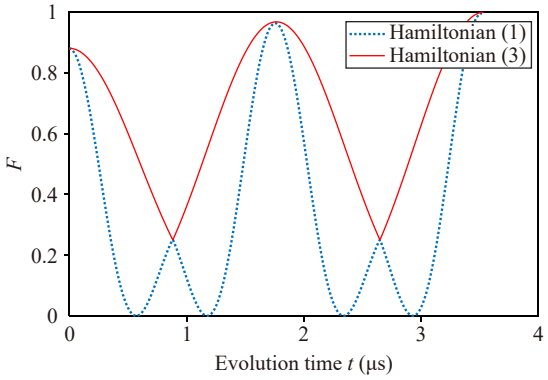

Fig. 6 Time evolution of the fidelity for the controlled-phase gate using the Hamiltonian (1) and Hamiltonian (3), respectively. The parameters are set to $N = 4$, $\delta/(2\pi) = 1\,\text{GHz}$, $\Delta/(2\pi) = 12\,\text{GHz}$, $g/(2\pi) = 700\,\text{MHz}$, and $\Omega_j/(2\pi) = 300\,\text{MHz}$. It can be seen that the two curves almost overlap at the final moment and reach the maximum value, confirming the validity of the Hamiltonian (3).

errors can be indirectly mitigated by increasing pulse segments, since the current GRAPE-based optimization has inherent robustness against such parameter variations and experimental imperfections. In addition, this method can also be extended to multi-qubit registers by cascading cavity-NV modules via optical fibers, and other solid-state emitters with superior optical properties, such as silicon-vacancy (SiV) centers [48, 92].

6 Conclusions

In conclusion, we have proposed a scheme for optimizing quantum gate operations by the GRAPE algorithm within a DFS. This scheme is applied to a system consisting of NV centers in diamond and a WGM microresonator. The advantage of our scheme lies in combining quantum optimal control theory with the protective properties of DFS. Through numerical optimization, we successfully find pulse sequences that can counteract specific errors. As applications, we implement high-fidelity controlled-phase and SWAP gates in a robust manner. The numerical simulation results demonstrate that our designed control pulses can effectively resist quasi-static noise, such as thermal noise and Rabi frequency errors. Furthermore, we have shown that increasing the number of discretized pulse segments is an effective means to enhance the robustness of the gate operations. Therefore, this work offers a promising approach for achieving high-fidelity and robust universal quantum computation in DFS.

Declarations The authors declare that they have no competing interests and there are no conflicts.

Acknowledgements Z.-C. S. was supported by the National Natural Science Foundation of China under Grant No. 62571129 and the Natural Science Foundation of Fujian Province under Grant No. 2025J01456. Y. X. was supported by the National Natural Science Foundation of China under Grant No. 11575045 and No. 11874114, the Natural Science Funds for Distinguished Young Scholar of Fujian Province under Grant No. 2020J06011, and a project from Fuzhou University under Grant No. JG2020001-2. Y.-H. C. was supported by the National Natural Science Foundation of China under Grant No. 12574386, the Fujian 100 Talents Program, and the Fujian Minjiang Scholar Program.

References

1. C. Monroe, Quantum information processing with atoms and photons, *Nature* 416(6877), 238 (2002)
2. C. Weedbrook, S. Pirandola, R. García-Patrón, N. J. Cerf, T. C. Ralph, J. H. Shapiro, and S. Lloyd, Gaussian quantum information, *Rev. Mod. Phys.* 84(2), 621 (2012)
3. F. Flamini, N. Spagnolo, and F. Sciarrino, Photonic quantum information processing: A review, *Rep. Prog. Phys.* 82(1), 016001 (2019)
4. S. Hawaldar, P. Shahi, A. L. Carter, A. M. Rey, J. J. Bollinger, and A. Shankar, Bilayer crystals of trapped ions for quantum information processing, *Phys. Rev. X* 14(3), 031030 (2024)
5. N. Gisin and R. Thew, Quantum communication, *Nat. Photonics* 1(3), 165 (2007)
6. K. Azuma, S. E. Economou, D. Elkouss, P. Hilaire, L. Jiang, H. K. Lo, and I. Tzitrin, Quantum repeaters: From quantum networks to the quantum internet, *Rev. Mod. Phys.* 95(4), 045006 (2023)
7. P. Zhao, W. Zhong, M. M. Du, X. Y. Li, L. Zhou, and Y. B. Sheng, Quantum secure direct communication with hybrid entanglement, *Front. Phys. (Beijing)* 19(5), 51201 (2024)
8. J. W. Ying, Y. B. Sheng, L. Zhou, and L. C. Kwek, A world-record achievement in the 100 kilometer practical quantum secure direct communication rate, *Front. Phys. (Beijing)* 20(3), 033401 (2025)
9. C. L. Degen, F. Reinhard, and P. Cappellaro, Quantum sensing, *Rev. Mod. Phys.* 89(3), 035002 (2017)
10. G. F. Xu, Nonadiabatic holonomic quantum computation based on nitrogen–vacancy centers, *Sci. China Phys. Mech. Astron.* 61(1), 010331 (2018)
11. F. Arute, K. Arya, R. Babbush, D. Bacon, J. C. Bardin, et al., Quantum supremacy using a programmable superconducting processor, *Nature* 574(7779), 505 (2019)
12. S. McArdle, S. Endo, A. Aspuru-Guzik, S. C. Benjamin, and X. Yuan, Quantum computational chemistry, *Rev. Mod. Phys.* 92(1), 015003 (2020)
13. C. Monroe, W. C. Campbell, L. M. Duan, Z. X. Gong, A. V. Gorshkov, P. W. Hess, R. Islam, K. Kim, N. M. Linke, G. Pagano, P. Richerme, C. Senko, and N. Y. Yao, Programmable quantum simulations of spin systems with trapped ions, *Rev. Mod. Phys.* 93(2), 025001 (2021)
14. K. Xu, H. J. Zhu, H. Zhu, G. F. Zhang, and W. M. Liu,

Charging and self-discharging process of a quantum battery in composite environments, *Front. Phys. (Beijing)* 18(3), 31301 (2023)
15. W. Feng, D. Shao, G. Q. Zhang, Q. P. Su, J. X. Zhang, and C. P. Yang, Quantum simulation of Hofstadter butterfly with synthetic gauge fields on two-dimensional superconducting-qubit lattices, *Front. Phys. (Beijing)* 18(6), 61302 (2023)
16. B. Cheng, X. H. Deng, X. Gu, Y. He, G. Hu, P. Huang, J. Li, B. C. Lin, D. Lu, Y. Lu, C. Qiu, H. Wang, T. Xin, S. Yu, M. H. Yung, J. Zeng, S. Zhang, Y. Zhong, X. Peng, F. Nori, and D. Yu, Noisy intermediate-scale quantum computers, *Front. Phys. (Beijing)* 18(2), 21308 (2023)
17. F. F. Du, X. M. Ren, M. Ma, and G. Fan, Qudit-based high-dimensional controlled-not gate, *Opt. Lett.* 49(5), 1229 (2024)
18. Z. G. Fan, X. S. Deng, Q. L. Tan, and F. F. Du, Linear-optics-based high-dimensional quantum gate with qudits, *Opt. Lett.* 50(18), 5771 (2025)
19. Z. Y. Xue and C. Y. Ding, Recent advances on nonadiabatic geometric quantum computation, *Front. Phys. (Beijing)* 21(3), 033202 (2026)
20. D. Suter and G. A. Álvarez, Colloquium: Protecting quantum information against environmental noise, *Rev. Mod. Phys.* 88(4), 041001 (2016)
21. M. Alam and S. Ghosh, Qnet: A scalable and noise-resilient quantum neural network architecture for noisy intermediate-scale quantum computers, *Front. Phys. (Lausanne)* 9, 755139 (2022)
22. K. Li, The qubit fidelity under different error mechanisms based on error correction threshold, *Front. Phys. (Lausanne)* 10, 893507 (2022)
23. P. Zanardi and F. Rossi, Quantum information in semiconductors: Noiseless encoding in a quantum dot array, *Phys. Rev. Lett.* 81(21), 4752 (1998)
24. D. A. Lidar, I. L. Chuang, and K. B. Whaley, Decoherence-free subspaces for quantum computation, *Phys. Rev. Lett.* 81(12), 2594 (1998)
25. D. A. Lidar, D. Bacon, and K. B. Whaley, Concatenating decoherence-free subspaces with quantum error correcting codes, *Phys. Rev. Lett.* 82(22), 4556 (1999)
26. D. Bacon, J. Kempe, D. A. Lidar, and K. B. Whaley, Universal fault-tolerant quantum computation on decoherence-free subspaces, *Phys. Rev. Lett.* 85(8), 1758 (2000)
27. X. Hu, F. Zhang, Y. Li, and G. Long, Optimizing quantum gates within decoherence-free subspaces, *Phys. Rev. A* 104(6), 062612 (2021)
28. G. Quiroz, B. Pokharel, J. Boen, L. Tewala, V. Tripathi, D. Williams, L. A. Wu, P. Titum, K. Schultz, and D. Lidar, Dynamically generated decoherence-free subspaces and subsystems on superconducting qubits, *Rep. Prog. Phys.* 87(9), 097601 (2024)
29. L. H. C. Vaecairn, J. T. Reilly, J. D. Wilson, S. B. Jäger, and M. Holland, Engineering tunable decoherence-free subspaces with collective atom–cavity interactions, *Phys. Rev. A* 111(3), 033718 (2025)
30. S. J. Glaser, U. Boscain, T. Calarco, C. P. Koch, W. K¨ockenberger, R. Kosloff, I. Kuprov, B. Luy, S. Schirmer, T. Schulte-Herbrüggen, D. Sugny, and F. K. Wilhelm, Training Schrödingers cat: Quantum optimal control, *Eur. Phys. J. D* 69(12), 279 (2015)
31. J. Li, X. Yang, X. Peng, and C. P. Sun, Hybrid quantum-classical approach to quantum optimal control, *Phys. Rev. Lett.* 118(15), 150503 (2017)
32. F. Sauvage and F. Mintert, Optimal control of families of quantum gates, *Phys. Rev. Lett.* 129(5), 050507 (2022)
33. R. Wu, Geometric approach to robust quantum control for time-varying noises, *Sci. China Phys. Mech. Astron.* 67(9), 290331 (2024)
34. X. Dong, X. Cao, W. L. Li, G. Zhang, Z. Peng, and R. B. Wu, Quantum optimal control theory for the shaping of flying qubits, *Phys. Rev. Appl.* 23(4), 044045 (2025)
35. T. Suzuki, Optimal control in nearly adiabatic two-level quantum systems via time-dependent resonance, *Phys. Rev. A* 111(5), L050201 (2025)
36. E. M. Fortunato, L. Viola, J. Hodges, G. Teklemariam, and D. G. Cory, Implementation of universal control on a decoherence-free qubit, *New J. Phys.* 4, 5 (2002)
37. D. Wei, J. Luo, X. Sun, X. Zeng, M. Zhan, and M. Liu, Realization of a decoherence-free subspace using multiple quantum coherences, *Phys. Rev. Lett.* 95(2), 020501 (2005)
38. Z. R. Zhang, C. W. Wu, C. Y. Li, H. Y. Dai, and C. Z. Li, Universal quantum computation in a decoherence-free subspace for collective relaxation with transmon qubits, *Phys. Rev. A* 87(6), 062325 (2013)
39. Z. Y. Xue, J. Zhou, and Z. D. Wang, Universal holonomic quantum gates in decoherence-free subspace on superconducting circuits, *Phys. Rev. A* 92(2), 022320 (2015)
40. Z. Li, M. J. Liang, and Z. Y. Xue, Time-optimal universal quantum gates on superconducting circuits, *Phys. Rev. A* 108(4), 042617 (2023)
41. L. Aolita, L. Davidovich, K. Kim, and H. Häffner, Universal quantum computation in decoherence-free subspaces with hot trapped ions, *Phys. Rev. A* 75(5), 052337 (2007)
42. T. Monz, K. Kim, A. S. Villar, P. Schindler, M. Chwalla, M. Riebe, C. F. Roos, H. Häffner, W. Hänsel, M. Hennrich, and R. Blatt, Realization of universal ion-trap quantum computation with decoherence-free qubits, *Phys. Rev. Lett.* 103(20), 200503 (2009)
43. P. A. Ivanov, U. G. Poschinger, K. Singer, and F. Schmidt-Kaler, Quantum gate in the decoherence-free subspace of trapped-ion qubits, *Europhys. Lett.* 92(3), 30006 (2010)
44. F. F. Du, G. Fan, and X. M. Ren, Kerreffect-based quantum logical gates in decoherence-free subspace, *Quantum* 8, 1342 (2024)
45. A. P. Liu, L. Y. Cheng, L. Chen, S. L. Su, H. F. Wang, and S. Zhang, Quantum information processing in decoherence-free subspace with nitrogen-vacancy centers coupled to a whispering-gallery mode microresonator, *Opt. Commun.* 313, 180 (2014)
46. F. Wang, Y. Y. Huang, Z. Y. Zhang, C. Zu, P. Y. Hou, X. X. Yuan, W. B. Wang, W. G. Zhang, L. He, X. Y. Chang, and L. M. Duan, Room-temperature storage of quantum entanglement using decoherence-free subspace in a solid-state spin system, *Phys. Rev. B* 96(13), 134314 (2017)

47. K. R. Koteswara Rao, and D. Suter, Level anticrossings of an NV center in diamond: Decoherence-free subspaces and 3D sensors of microwave magnetic fields, arXiv: 1908.07796 (2019)
48. G. Fan, H. Z. Niu, Q. L. Tan, and F. F. Du, A computation-enhanced high-dimensional quantum gate for silicon-vacancy spins, *Adv. Quantum Technol.* 8(10), 2500167 (2025)
49. X. Rong, J. Geng, F. Shi, Y. Liu, K. Xu, W. Ma, F. Kong, Z. Jiang, Y. Wu, and J. Du, Experimental fault-tolerant universal quantum gates with solid-state spins under ambient conditions, *Nat. Commun.* 6(1), 8748 (2015)
50. L. Robledo, L. Childress, H. Bernien, B. Hensen, P. F. A. Alkemade, and R. Hanson, High-fidelity projective readout of a solid-state spin quantum register, *Phys. Rev. Lett.* 105, 177403 (2011)
51. C. G. Yale, B. B. Buckley, D. J. Christle, G. Burkard, F. J. Heremans, L. C. Bassett, and D. D. Awschalom, All-optical control of a solid-state spin using coherent dark states, *Nat. Phys.* 10, 945 (2014)
52. T. J. Wang and C. Wang, Universal hybrid three-qubit quantum gates assisted by a nitrogen-vacancy center coupled with a whispering-gallery-mode microresonator, *Phys. Rev. A* 90(5), 052310 (2014)
53. X. Zhang and C. Orphal-Kobin, Coherent microwave, optical, and mechanical quantum control of spin qubits in diamond, *Adv. Quantum Technol.* 8(2), 2300432 (2025)
54. P. E. Barclay, K. M. C. Fu, C. Santori, A. Faraon, and R. G. Beausoleil, Hybrid nanocavities for resonant enhancement of color center emission in diamond, *Nano Lett.* 11, 3217 (2011)
55. A. Faraon, P. E. Barclay, C. Santori, K. M. C. Fu, and R. G. Beausoleil, Resonant enhancement of the zero-phonon emission from a colour centre in a diamond cavity, *Nat. Photonics* 5(5), 301 (2011)
56. S. Johnson, A. Sipahigil, M. D. Lukin, and M. Lončar, Progress in diamond quantum photonics for distributed quantum networks, *Prog. Quantum Electron.* 52, 62 (2017)
57. F. F. Du, M. Ma, and Q. Tan, Heralded interconversion between hyperentangled W state and hyperentangled KLM state assisted by nitrogen vacancy centers coupled with microresonators, *Sci. Rep.* 15(1), 2505 (2025)
58. P. Doria, T. Calarco, and S. Montangero, Optimal control technique for many-body quantum dynamics, *Phys. Rev. Lett.* 106(19), 190501 (2011)
59. P. M. Poggi and D. A. Wisniacki, Optimal control of many-body quantum dynamics: Chaos and complexity, *Phys. Rev. A* 94(3), 033406 (2016)
60. S. van Frank, M. Bonneau, J. Schmiedmayer, S. Hild, C. Gross, M. Cheneau, I. Bloch, T. Pichler, A. Negretti, T. Calarco, and S. Montangero, Optimal control of complex atomic quantum systems, *Sci. Rep.* 6(1), 34187 (2016)
61. R. Roloff, M. Wenin, and W. Ptz, Optimal control for open quantum systems: Qubits and quantum gates, *Phys. Rev. A* 79, 013819 (2009)
62. Y. Chen, Y. Hao, Z. Wu, B. Y. Wang, R. Liu, Y. Hou, J. Cui, M. H. Yung, and X. Peng, Accelerating quantum optimal control through iterative gradient-ascent pulse engineering, *Phys. Rev. A* 108(5), 052603 (2023)
63. N. Khaneja, T. Reiss, C. Kehlet, T. Schulte-Herbrüggen, and S. J. Glaser, Optimal control of coupled spin dynamics: Design of NMR pulse sequences by gradient ascent algorithms, *J. Magn. Reson.* 172(2), 296 (2005)
64. B. L'eon, F. E. Curtis, and J. Nocedal, Optimization methods for large-scale machine learning, *SIAM Rev.* 60(2), 223 (2018)
65. T. C. Kaspar, T. Droubay, and J. E. Jaffe, ZnO/Sn: In_2O_3 and ZnO/CdTe band offsets for extremely thin absorber photovoltaics, *Appl. Phys. Lett.* 99(26), 263504 (2011)
66. L. S. Theis, F. Motzoi, F. K. Wilhelm, and M. Saffman, High-fidelity Rydberg-blockade entangling gate using shaped, analytic pulses, *Phys. Rev. A* 94(3), 032306 (2016)
67. T. J. Green, J. Sastrawan, H. Uys, and M. J. Biercuk, Arbitrary quantum control of qubits in the presence of universal noise, *New J. Phys.* 15(9), 095004 (2013)
68. L. Gyongyosi and S. Imre, Decentralized base-graph routing for the quantum internet, *Phys. Rev. A* 98(2), 022310 (2018)
69. J. R. Johansson, P. D. Nation, and F. Nori, QuTiP$_2$: A Python framework for the dynamics of open quantum systems, *Comput. Phys. Commun.* 184(4), 1234 (2013)
70. M. H. Goerz, E. J. Halperin, J. M. Aytac, C. P. Koch, and K. B. Whaley, Robustness of high-fidelity Rydberg gates with single-site addressability, *Phys. Rev. A* 90(3), 032329 (2014)
71. N. Leung, M. Abdelhafez, J. Koch, and D. Schuster, Speedup for quantum optimal control from automatic differentiation based on graphics processing units, *Phys. Rev. A* 95(4), 042318 (2017)
72. M. Bukov, A. G. R. Day, D. Sels, P. Weinberg, A. Polkovnikov, and P. Mehta, Reinforcement learning in different phases of quantum control, *Phys. Rev. X* 8(3), 031086 (2018)
73. M. Y. Niu, S. Boixo, V. N. Smelyanskiy, and H. Neven, Universal quantum control through deep reinforcement learning, *npj Quantum Inf.* 5, 33 (2019)
74. M. W. Doherty, N. B. Manson, P. Delaney, F. Jelezko, J¨. Wrachtrup, and L. C. L. Hollenberg, The nitrogen-vacancy colour centre in diamond, *Phys. Rep.* 528(1), 1 (2013)
75. E. Togan, Y. Chu, A. S. Trifonov, L. Jiang, J. Maze, L. Childress, M. V. G. Dutt, A. S. Sørensen, P. R. Hemmer, A. S. Zibrov, and M. D. Lukin, Quantum entanglement between an optical photon and a solid-state spin qubit, *Nature* 466(7307), 730 (2010)
76. D. F. James and J. Jerke, Effective Hamiltonian theory and its applications in quantum information, *Can. J. Phys.* 85(6), 625 (2007)
77. J. Zhou, W. C. Yu, Y. M. Gao, and Z. Y. Xue, Cavity QED implementation of non-adiabatic holonomies for universal quantum gates in decoherence-free subspaces with nitrogen–vacancy centers, *Opt. Express* 23(11), 14027 (2015)
78. E. Brion, L. H. Pedersen, K. Mølmer, S. Chutia, and M. Saffman, Universal quantum computation in a neutral-

atom decoherence-free subspace, *Phys. Rev. A* 75(3), 032328 (2007)
79. Z. C. Shi, J. T. Ding, Y. H. Chen, J. Song, Y. Xia, X. X. Yi, and F. Nori, Supervised learning for robust quantum control in composite-pulse systems, *Phys. Rev. Appl.* 21(4), 044012 (2024)
80. E. T. Güldeste and C. Bulutay, Wavelet resolved coherence beating in the Overhauser field of a thermal nuclear spin ensemble, *Phys. Rev. B* 105(7), 075202 (2022)
81. S. Lin, C. Weng, Y. Yang, J. Zhao, Y. Guo, J. Zhang, L. Lou, W. Zhu, and G. Wang, Temperature-dependent coherence properties of NV ensemble in diamond up to 600 K, *Phys. Rev. B* 104(15), 155430 (2021)
82. M. R. Yun, F. Q. Guo, L. L. Yan, E. Liang, Y. Zhang, S. L. Su, C. X. Shan, and Y. Jia, Parallelpath implementation of nonadiabatic geometric quantum gates in a decoherence-free subspace with nitrogen-vacancy centers, *Phys. Rev. A* 105(1), 012611 (2022)
83. B. T. Torosov and N. V. Vitanov, Smooth composite pulses for high-fidelity quantum information processing, *Phys. Rev. A* 83(5), 053420 (2011)
84. G. T. Genov, D. Schraft, T. Halfmann, and N. V. Vitanov, Correction of arbitrary field errors in population inversion of quantum systems by universal composite pulses, *Phys. Rev. Lett.* 113(4), 043001 (2014)
85. Z. C. Shi, H. N. Wu, L. T. Shen, J. Song, Y. Xia, X. X. Yi, and S. B. Zheng, Robust single-qubit gates by composite pulses in three-level systems, *Phys. Rev. A* 103(5), 052612 (2021)
86. A. Ruschhaupt, X. Chen, D. Alonso, and J. G. Muga, Optimally robust shortcuts to population inversion in two-level quantum systems, *New J. Phys.* 14(9), 093040 (2012)
87. D. Daems, A. Ruschhaupt, D. Sugny, and S. Guérin, Robust quantum control by a single-shot shaped pulse, *Phys. Rev. Lett.* 111(5), 050404 (2013)
88. Y. Zheng, Z. Fang, S. Liu, Y. Cheng, and X. Chen, High-q exterior whispering-gallery modes in a double-layer crystalline microdisk resonator, *Phys. Rev. Lett.* 122(25), 253902 (2019)
89. Q. H. Song, Emerging opportunities for ultra-high Q whispering gallery mode microcavities, *Sci. China Phys. Mech. Astron.* 62(7), 074231 (2019)
90. N. Acharyya and G. Kozyreff, Large q factor with very small whispering-gallery-mode resonators, *Phys. Rev. Appl.* 12(1), 014060 (2019)
91. G. Balasubramanian, P. Neumann, D. Twitchen, M. Markham, R. Kolesov, N. Mizuochi, J. Isoya, J. Achard, J. Beck, J. Tissler, V. Jacques, P. R. Hemmer, F. Jelezko, and J. Wrachtrup, Ultralong spin coherence time in isotopically engineered diamond, *Nat. Mater.* 8(5), 383 (2009)
92. A. Sipahigil, K. D. Jahnke, L. J. Rogers, T. Teraji, J. Isoya, A. S. Zibrov, F. Jelezko, and M. D. Lukin, Indistinguishable photons from separated silicon-vacancy centers in diamond, *Phys. Rev. Lett.* 113(11), 113602 (2014)